P3.27

INTERACTION OF TRAPPED LEE-WAVES AND THE CONVECTIVE BOUNDARY LAYER

Rolf F. Hertenstein and Gregory S. Poulos

Colorado Research Associates, a division of NWRA, Boulder, Colorado

1. INTRODUCTION

Trapped mountain waves have been subject of many studies over the past several decades. Recently, increased interest has surfaced in the non-stationarity of trapped mountain waves (Nance and Durran 1998; Ralph et al. 1997 and references therein). Three possibilities exist for nonstationarity, changes in upstream conditions, wave-wave interactions, or an evolving atmospheric boundary layer (ABL).

Our focus here is on the interaction between trapped lee waves and the convective boundary layer (CBL), with the goal of quantifying the mutual interaction between trapped lee waves and the CBL. To this end we ran three simulations. First, a simulation of trapped lee waves with no surface heating is carried out. Second, a simulation is run in which a CBL is allowed to develop with no ambient wind. Finally, both trapped lee waves and the CBL are allowed to develop simultaneously.

2. EXPERIMENTAL DESIGN

The mesoscale model used was the Regional Atmospheric Modeling System, (RAMS, Pielke et al. 1992). The two-dimensional simulations feature 1700 points in the horizontal with 150m grid spacing. In the vertical, 130 points were used with constant 50m spacing to a height of 1800m, then stretched to a maximum of 150m. A skewed 1500m high topographical barrier with upwind half-width of 20 km, and downwind half-width of 10 km is utilized on all runs. All simulations feature a no-slip lower boundary and all are run with no moisture.

The initial sounding emulates that used by Doyle and Durran (2002) (hereafter DD) and represents an average of three soundings in and near Colorado on 3 March 1991. We note that the simulations are not meant to replicate the actual conditions occurring on this day. The lee-wave-only simulation (LO) is initialized with the temperature and wind profile and is then run for 6 hours with no surface heat flux (soil model and radiation parameterization off). The CBL-only simulation (CO) is initialized with the same temperature profile, but with no wind at any level. The model run is started two hours before local sunrise, then is run for 14 hours, with soil model and radiation parameterizations active, allowing evolution of surface cooling and heating. The final simulation (LC) uses both the temperature and wind profile from the sounding. As in CO, the model is initialized two hours before local sunrise, then run for 14 hours with the soil model and radiation parameterization active.

3. RESULTS

An overview of each run is shown by vertical velocity (*w*) at 1025 m in the *x-t* plane (Figures 1-3). Note the different time scale used for LO vs. CO and LC since the former was run only for 6 hours. Also, only the the domain downstream of the mountain is shown for LO since the upstream fields change little.

The primary wave forms in LO within the first hour (Fig. 1) and remains quasi-stationary to the end of the simulation at 6 hours. During the period between 1.5 and 6 hours subsequent trapped waves form downstream, and similar to the primary wave, these downstream oscillations remain quasi-stationary once formed. Between 3 and 6 hours, the distance from the mountain to the primary updraft first increases by 1.5 km, then steadily decreases by 3.1 km. In addition, the amplitude varies by 105m over this time. Similar behavior has been noted by Nance and Durran (1998) in the absence of changing upstream conditions.

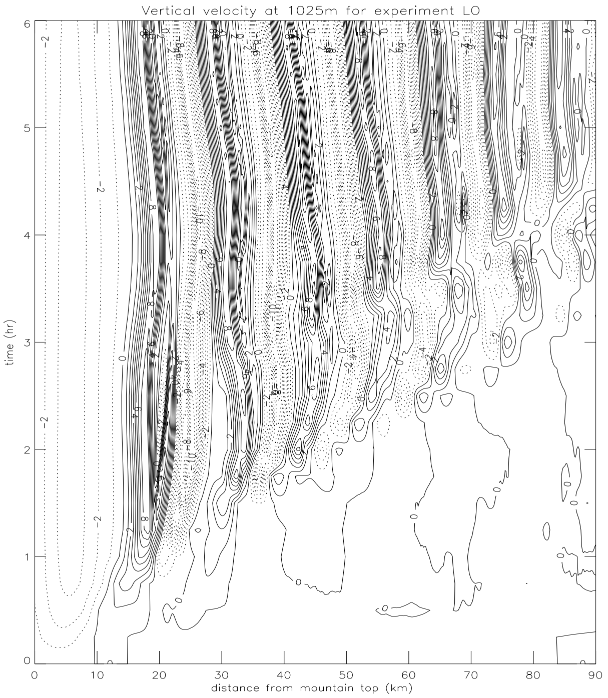

Figure 1. Vertical velocity at 1025 m for Experiment LO. Contour interval 0.5 ms^{-1}. Mountain top is located at x = 0 km.

---

* *Corresponding author address:* Rolf F. Hertenstein, Colorado Research Associates, a division of NWRA,, 3380 Mitchell Lane, Boulder, CO 80301, herten@cora.com

Potential temperature (θ) and horizontal wind (u) at 6 h into the simulation show that under each wave crest, a well-mixed rotor has formed (not shown), similar to DD. A lee slope downdraft reaches 3.5 ms^{-1} while w in subsequent lee waves are approximately +8 and -9 ms^{-1}. Near-surface easterly flow under the primary rotor is 8 ms^{-1}.

Downslope winds reach almost 21 ms^{-1} along the lee slope. Downstream of the primary downdraft, the sign of u oscillates between negative under the rotors and positive in wave troughs. Locations of positive and negative u undulate in synergy with w.

For CO, only very weak w is seen at 1025 m (Fig. 2) until several hours after local sunrise while near-surface u responds to the evolving diurnal cycle. By sunrise, a shallow katabatic flow has developed with a maximum velocity of 1.4 ms^{-1} on the east-facing slope and -1.8 ms^{-1} on the shallower west-facing slope. Over the next several hours, solar heating warms the east-facing slope, and by 6.5 hours, easterly upslope flow of about 2.5 ms^{-1} is seen over the upper half of the east-facing slope, while westerly flow is seen along the lower slope and into the adjacent plains. The transition from katabatic to upslope flow occurs rapidly, within 30 minutes. At this time the katabatic flow on the west-facing slope has strengthened from the earlier time.

Strengthening easterly upslope combined with greater insolation near the mountain top leads to the first strong (i.e., greater than 1 ms^{-1}) convective cells there by 8 h. Upslope flow rapidly develops on the west-facing slope after this time; the ensuing convergence zone focuses convection near the mountain top for the remainder of the simulation. It is interesting to note that the convergence zone remains west of the peak since the easterly upslope develops first. In synoptically realistic situations, the location of this convergence zone will depend on the direction and strength of the cross-mountain pressure gradient. Within an hour after convection is triggered along the upper slopes, it also fires along the lower portions of the slope, then progressively further eastward into the plains, so by 11 hours (mid-afternoon) the entire boundary layer, both mountain and plains, has become convectively mixed. An area of suppressed convection is apparent adjacent to the upper slopes. Convergence-enhanced convection over the mountain is about 2 ms^{-1} stronger and reaches about 500 m higher than convective cells beyond the suppression zone in the plains. The deeper convective cells near the mountain top perturbs the overlying stable layer and produces small amplitude waves with wavelength O(4 km). By this time a mountain-plains solenoid is well formed, with easterly flow (O[5 ms^{-1}]) below about 1500-2000m along the entire domain east of the mountain top (with the exception of a small weak areas of westerly flow associated with individual convective plumes), while return westerly flow (O[6 ms^{-1}]) is seen above this region to about 3 km in the vicinity of the initial elevated inversion.

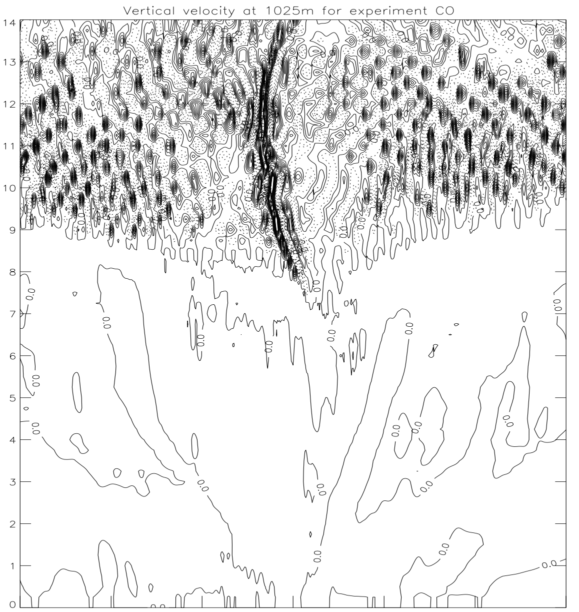

Figure 2. As in Fig. 1 except for Experiment CO. Contour interval 1 ms^{-1}.

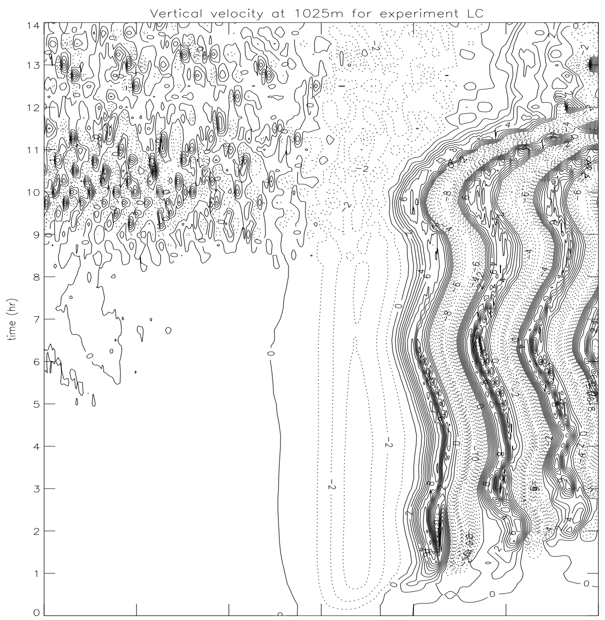

Figure 3. As in Fig. 1 except for Experiment LC. Contour interval 1 ms^{-1}.

Simulation LC (Fig. 3) shows a series of trapped waves forming in the first few hours. Nonstationarity is evident as the location of the primary updraft varies by a maximum of 4.2 km between 2 and 9 h. Convective cells (> 1.0 ms^{-1}) form upwind of the mountain after 9 h while lee slope downdrafts suppress convection there. Approximately 1 hour after convection becomes active on the upstream side of the mountain, the trapped waves propagate rapidly downstream and are largely destroyed. Convective cells do not form to the lee of the mountain as near-surface, 20 ms^{-1} downslope winds spread into the plains as the trapped waves propagate away.

The trapped waves in LO and LC are qualitatively similar to 6 h. Subtle differences do appear by 3 h, at which time surface cooling creates a shallow stable layer in LC, with surface temperatures approximately 2.5 C cooler along the lee slope in LC. The low-level cooling modifies the trapped wave; the amplitude in LO is about 10% greater while the wavelength between the first and second harmonic is approximately 20% greater than LC. The shorter wavelength in LC can be qualitatively understood since cooling increases the average stability below the mountain top. Beyond the second wave LC displays increased small-scale spatial and temporal structure. By 6 hours surface heat fluxes have reached about 50 Wm^{-2} along the lee slope and into the adjacent plains. In addition, the primary updraft in LC is seen to oscillate 1.1 km more than in LO; both surface cooling and heating have lead to increased nonstationarity.

Horizontal vorticity and negative values of *u* under the rotor at 6 h for LO and LC also show differences in wavelength between the two experiments. The rotor depth was found to be 100 m higher for LO than LC, though the rotor strength (as determined by the magnitude of horizontal vorticity) appears stronger in the latter. Before sunrise in LC, surface cooling has lead to increased vertical shear, which is the larger term in the horizontal vorticity. Thus in LC, primary rotor leading edge relative vorticity reaches 0.04 s^{-1}, almost twice as strong as LO, with stronger reversed flow under the rotor (-9.88 vs. -8.16 ms^{-1}). In addition, a region of horizontal vorticity greater than 0.02 s^{-1} is seen within the rotor circulation of LC, a feature lacking in LO. It is interesting to note that unlike DD, rotor depth *decreases* with the addition of heating. For LO, the rotor depth increases 200 m between 3 and 6 h. After 6 h, heating increases steadily from 50 to 300-500 Wm^{-2} while rotor depth in LC first remains unchanged then decreases substantially as the lee wave wavelength increases. Appearantly, the spatial and temporal distribution of surface heating effect the rotor structure.

Between 6 and 9 h, very little convection forms on the mountain top or upper slopes in LC in contrast to CO (cf. Figs. 2 and 3). Thus, it becomes obvious that the flow over the mountain first modulates convection on the lee side. The near-mountain-top convergence zone that forms in CO because of diurnal upslope flow is completely lacking in LC. By 10 h, convection upstream of the mountain is similar in both simulations, with the exception of a 10 km wide region of somewhat supressed convection west of the convergence zone in CO. Convection upstream of the mountain tends to be 1-2 ms^{-1} weaker in LC compared to CO likely due to better ventilation. On the eastern slope, each simulation receives the same isolation, but convection is suppressed in LC due to the 3.5 ms^{-1} downdraft along the lee slope.

By 11 hours (mid-afternoon), surface heat fluxes vary considerably between 100 and 500 Wm^{-2} in LC, especially to the lee of the mountain, and the influence of surface heating has begun to dramatically alter the lee waves. The primary updraft has weakened to 5 ms^{-1} and is now located 23 km from the mountain crest. The amplitudes of other harmonics have weakened and have begun to propagate downstream. This trend continues and by 12 hours (about an hour before local sunset) a weaker primary wave is seen 30-40 km from the mountain crest. Other harmonics have propagated down stream. The downslope flow during this period has increased (from 22 to 24 ms^{-1}), has moved further to the east and a broad region exceeding 20 ms^{-1} is now located 19 to 35 km from the mountain crest. The fairly sudden departure from a quasi-steady state appears to be caused by a deep mixed layer forming on the windward side of the mountain due to surface heating. Thus, we have nonstationarity due to changes in the upstream environment, but those changes are due to the diurnal cycle rather than changes in the synoptic pattern.

Tendencies from the model momentum equations were written out every time step (0.5 s). We first consider a model grid point located along the lee slope at x = 9 km. For LO, *u* remains relatively steady between 3 and 6 h due to positive pressure gradient (0.03 ms^{-2}) balanced by negative advection (-0.023 ms^{-2}) and diffusion (-0.007 ms^{-2}). A similar force balance occurs during LC before convection deepens on the windward mountain side. Thereafter, the force balance is disrupted with oscillations occuring in the forcing terms with a frequency of approximately 30 min as the waves break down. In the final two hours of the simulation, both *u* and its tendencies display small, non-preiodic variability resembling turbulent flow.

Next, a model grid point (x = 25.8 km) was chosen to better understand the near-surface dynamics in the vicinity of the primary rotor. The point was chosen because nonstationarity causes it first to be located under the rotor, then it is located in westerly flow in the primary wave trough (i.e., downstream of the primary wave) during LO. Magnitudes of the tendency terms are first similar to the lee-slope point (x = 9 km) but the sign of all terms is opposite. As the wavelength shifts, the grid point is under the influence of the primary wave trough. Tendencies change sign, and initially increase in magnitude threefold. By contrast, after convection begins in LC, the tendencies oscillate in sign and magnitude as the grid point experinces rapid change from primary trough, to rotor, primary updraft, and finally, the extended downslope winds.

4. SUMMARY AND CONCLUSIONS

One possible cause of nonstationarity, i.e., the interaction between lee waves and the evolving CBL, was explored via a series of idealized two-dimensional simulations. Trapped-wave-only and CBL-only simulations produced results which were consistent with earlier studies. The third, a combined trapped-wave and CBL simulation, first produced quasi-stationary lee waves which later propagate away downstream as the CBL becomes fully developed. Overall, the well devloped CBL windward of the mountain barrier deepens with time, then advects over the mountain barrier, dramatically modifying the mountain-top stability and causing the trapped waves to propagate downstream. As this occurs, near-surface downslope winds spread into the Plains. The flow over the mountains and trapped waves influence the evolution of the CBL to the lee of the mountain as well. No well-developed convective cells form on the lee slopes nor in the adjacent Plains during any part of the simulation.

Comparing the trapped-wave-only and CBL-only simulations with the combined simulation, our conclusions are as follows:

1. The addition of surface cooling followed by heating first modifies the trapped-wave wavelength and amplitude. This has ramifications for mountain-wave prediction, e.g., when considering overlying high cloud cover which can reduce both night-time long-wave cooling and daytime shortwave heating. In addition, the turbulence budget is altered as was seen in differences in the rotor structure due to heating.

2. During the morning and early afternoon, the flow over topography and trapped waves modify the CBL. Upstream of the mountain peak, increased flow leads to weaker convective cells there, though number and distribution of cells appear similar. Downstream of the mountain peak, the downslope winds and trapped waves prevent organized convective cells from developing at all.

3. During the mid to later afternoon, the evolving CBL upstream of the mountain peak eventually deepens to a height exceeding the peak, leading to the destruction of the trapped waves downstream. An associated effect is an eastward extension of the near-surface downslope winds compared to the morning hours.

Since these experiments represent a very limited number of possible scenarios, it is important to avoid generalizing based on these three simulations alone. There is a broad spectrum of possible mountain wave forms, from trapped to the vertically-propagating waves. In addition, the CBL will evolve differently depending on many factors, e.g., time of year, ground cover and soil moisture, etc. For instance, the surface heating applied to a lee-wave simulation by Doyle and Durran (2002) emulated a situation in which the region upstream of the mountain peak remained cloud covered, as also often occurs. Their simulated rotors evolved differently from the scenario presented here. Evolving ambient conditions due to changing synoptics has obviously not been considered here. Finally, geographical locations, details of the topography itself, and three-dimensional flows and surface heating must play a significant role. Nevertheless, the results presented here are a useful step in quantifying the complex, nonlinear interaction between mountain waves and the atmospheric boundary layer.

5. ACKNOWLEDGMENTS

The authors acknowledge the support of the national Science Foundation ATM-9713073 and ATM-9816160.

6. REFERENCES

Pielke, R.A., W.R. Cotton, R.L. Walko, C.J. Tremback, W.A. Lyons, L.D. Grasso, M.E. Nicholls, M.D. Moran, D.A. Wesley, T.J. Lee, and J.H. Copeland, 1992: A comprehensive meteorological modeling system - RAMS. *Meteor. Atmos. Phys.*, **49**, 69-91.

Doyle J.D. and D.R. Durran, 2002: The dynamcis of mountain-wave-induced rotors. *J. Atmos.Sci.*, **59**, 186-201.

Nance L.B. and D.R. Durran, 1998: A modeling study of nonstationary traped mountain lee waves. Part II: Nonlinearity *J. Atmos.Sci.*, **55**, 1429-1445.

Ralph F.M., P.J. Neiman, T.L. Keller, D. Leivnson, and L. Fedor, 1997: Observations, simulations, and analysis of nonstationary trapped lee waves. *J. Atmos.Sci.*, **54**, 1308-1333.